Int J Disaster Risk Sci (2015) 6:250–266
DOI 10.1007/s13753-015-0058-1

www.ijdrs.com
www.springer.com/13753

ARTICLE

Measurement of Anomalous Radon Gas Emanation Across the Yammouneh Fault in Southern Lebanon: A Possible Approach to Earthquake Prediction

Mohammed A. Kobeissi[1] · Francisco Gomez[2] · Charles Tabet[3]

Published online: 11 September 2015

Abstract The eastern Mediterranean region is an active tectonic setting that includes the Dead Sea Transform Fault, which forms the boundary between the African and the Arabian Plates and crosses Lebanon from south to north, striking in a restraining bend around 25–30°NE. The major structural feature in Lebanon is the Yammouneh Fault, which reaches to Syria and southern Turkey in a north–south direction. Measurements of radon gas concentration and exhalation rates in two locations along the southern segment of the Yammouneh Fault in south Lebanon were performed. Two profiles in the El-Khiam basin and Blat pull-apart basin and perpendicular to the Yammouneh Fault trace were analyzed. An approximate fault width 25–30 m wide was determined in the El-Khiam study area. Temporal increase of radon concentration was measured and correlated with stress/strain tectonic activity and stress drops along the studied fault segment boundary. Anomalous variable radon concentrations were detected during one of the measurements where an earthquake occurred in the region of Tiberias Lake in northern Palestine along the Yammouneh Fault in the study area. Measurements of radon concentration along a station's profile in Blat village did not show any radon anomalous variation due to the discontinuity along the fault (pull-apart), and possible absence of stress and energy accumulation along the Yammouneh Fault line in that location.

Keywords CR-39 · Detector · Earthquake prediction · Exhalation rate · Lebanon · Radon · Stress/strain

1 Introduction

Lebanon straddles the boundary between the African and Arabian Plates along the Yammouneh Fault, which constitutes the middle segment (restraining bend) of the Dead Sea transform fault (DSTF). The DSTF enters south Lebanon through Galilee and spreads into five major faults as shown in Fig. 1. Also shown on map A of Fig. 1 is the Cypriote Arc, which delimits part of the subduction zone between the African and Eurasian plates. The most important fault for this study is the Yammouneh Fault, the only fault that transits the length of Lebanon, crosses Syria where it is known as the Ghab Fault (Ghab F. in Fig. 1 map B) and reaches southern Turkey (Freund et al. 1970; McKenzie 1972). The other faults are the Roum Fault, the Rachaya Fault, the Hasbaya Fault, and the Serghaya Fault (Walley 1988). The locations of these faults and other structures are shown in Fig. 1. Four of the five faults are considered active: the Yammouneh, Roum, Rachaya, and Serghaya faults.

Evaluation of the seismic hazard should take into consideration the high slip rate, 4–6 mm year^{-1}, along the Yammouneh Fault, which is the source of the most frequent earthquakes in Lebanon, with a quasi-periodic recurrence of large earthquakes of about 1020 years (Nemer, Gomez et al. 2008) as compared with 1.4 mm year^{-1} slip rate along the Serghaya Fault, which pierces through

✉ Mohammed A. Kobeissi
makobeissi@yahoo.com

[1] Lebanese Atomic Energy Commission, Lebanese National Council for Scientific Research, Airport Road, Beirut, Lebanon

[2] Department of Geological Sciences, University of Missouri, Columbia, MO 65211, USA

[3] Lebanese National Council for Scientific Research, Beirut, Lebanon

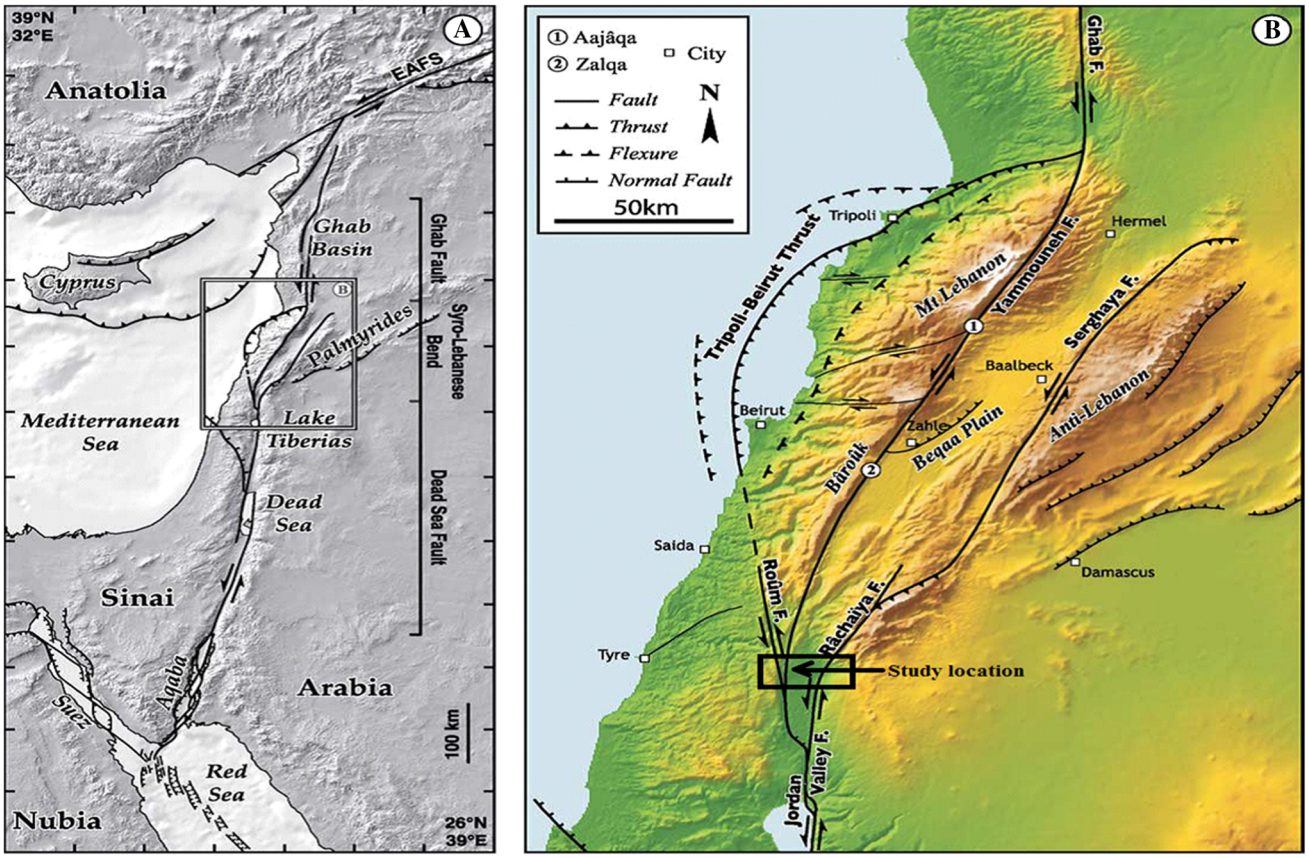

Fig. 1 **A** Map of Levant fault system. *Box* shows limits of map **B** presenting the active faults of the Lebanese restraining bend (Daeron et al. 2004)

the Anti-Lebanon range and has a recurrence period of approximately 1300 years (Gomez et al. 2003).

The geological nature and structure of DSTF has been investigated by many researchers worldwide (Walley 1988; Butler et al. 1998; Butler and Spencer 1999; Beydoun 1999; Meghraoui et al. 2003; Gomez et al. 2003, 2006, 2007). In addition, studies of the seismicity and tectonic activity of the DSTF, including its branching faults within Lebanese territory, have been carried out by Mohamad et al. (2000), Gomez et al. (2001), Tapponnier et al. (2001), Meghraoui et al. (2003), Nemer and Meghraoui (2006), Reilinger et al. (2006), Nemer, Meghraoui et al. (2008), Alchalbi et al. (2009), and Palano et al. (2013).

Presently, earthquake prediction is based on the periodicity of earthquakes based on historical events (Plassard and Kogoj 1981; Ambraseys and Melville 1988), which lacks accuracy. Recently new experimental methodology has been applied to predict earthquakes based on the emission of soil gases in the Earth's crust in the vicinity of geological faults (Yang et al. 2003; Erees et al. 2007; Papp et al. 2008; Kuo et al. 2009; Walia et al. 2009; Richon et al. 2010; Baykut et al. 2011; Bhongsuwan et al. 2011), as is done in the present study.

Because Lebanon is embedded partly in the Dead Sea fault system (DSFS), it has been subject to many destructive earthquakes throughout its history (Darawcheh et al. 2000; Daeron et al. 2004, 2005, 2007). Table 1 presents some recorded AD seismic events that have affected Lebanon.

The Yammouneh Fault, shown in Fig. 1, represents the most important structure because it connects the southern and the northern parts of the DSFS. This fault has a strike-slip displacement of 4–6 mm year^{-1}, while the Roum Fault shows a strike-slip rate of 1 mm year^{-1} (Gomez et al. 2003; Daeron et al. 2004; Nemer and Meghraoui 2006; Gomez et al. 2007). A recent study by Gomez et al. (2007) showed that the Yammouneh Fault accommodates most of the expected strike-slip motion, which indicates that this fault is accumulating strain. These authors deduce that the fault's present day lack of seismicity is likely a reflection of the slow rate of strain accumulation in a locked fault system. Such strain accumulation is a concern for potential future earthquakes along the Yammouneh Fault, which has

Table 1 Historical occurrence of earthquakes in Lebanon

Date of earthquakes	Magnitude[a]	Reference
9 July 551	7.5	Elias et al. (2007)
20 May 1202	7.5	Daeron et al. (2005)
30 October 1759	6.7	Daeron et al. (2005)
25 November 1759	7.4	Daeron et al. (2005)
27 September 1918	6.80	Plassard and Kogoj (1981)
16 March 1956	6.3 and 6.1	Khair (2001)
21 March 1997	5.6 and 5	Khair (2001)
15 February 2008	5.1	European-Mediterranean Seismological Center (n.d.)

[a] Magnitude of the historical earthquakes was estimated from the damage caused by these earthquakes as mentioned by historians or survivors at that time

a historical record of producing large earthquakes in Lebanon with magnitudes of around 7.5 on the Richter scale (Sbeinati et al. 2005), with a recurrence period ranging from 800 to 1000 years.

The Rachaya Fault splays from the eastern bounding fault basin and extends along the western Anti-Lebanon range. It runs approximately 45 km along that fault line and extends through the village of Chebaa, which is located at the south end of Anti-Lebanon and at the west side of Mount Hermon. This fault has a clear and noticeable trace along its entire length (Nemer, Meghraoui et al. 2008). Several studies of the tectonic activities of geological faults in Lebanon have been conducted, but investigation of the nature of the stresses, strains, and energy accumulation along the faults planes were not undertaken.

Based on contemporary concern about earthquake impacts, it is desirable to undertake a different approach to understanding and predicting seismic activity in Lebanon. Our focus in this research is on the southern segment of the Yammouneh Fault in south Lebanon as indicated in Fig. 1, map B.

In the present study we use the temporal variation of radon gas, Rn-222, discussed in Sect. 2.1 and referred to in the text as Rn, by measuring Rn emanation from the subsurface near the fault trace as has been done by many researchers worldwide (Yang et al. 2003; Walia et al. 2005; Papp et al. 2008; Kuo et al. 2009; Walia et al. 2009; Richon et al. 2010; Baykut et al. 2011; Bhongsuwan et al. 2011). The variability of radon gas concentrations due to seismic activity along a fault plane boundary shows positive results related to the stress and strain behavior of the faults. Careful study of this relationship can be a way to verify stress/strain and energy accumulation along the Yammouneh Fault system, as stated by Gomez et al. (2007).

In the present research work, the borehole and the ditch excavation techniques were used. To detect Rn gas, we adopted the solid state nuclear track detector (SSNTD) CR-39, which records cumulative Rn alpha tracks. The seismic activity along the Yammouneh Fault is a part of a long-term investigation of faults that cut through the Lebanese geological and geomorphological picture.

2 Methodology and Experimental Procedure

The choice of radon gas is due to its physical properties as inert gas and its emanation from the Earth's subsurface near the fault trace. These characteristics and properties are combined with the use of boreholes and ditches (trenches) dug across the fault trace as described in the following sections.

2.1 Radon Gas and Its Use in Detecting Seismic Activity

Many investigators have used Rn measurements to determine seismic activity due to Rn being a noble radioactive gas and chemically inert. Radon gas is a result of the decay chain of the radioactive isotope of Uranium, U-238, and is the daughter (progeny) of the radioactive radium Ra-226 (Ra). Radon gas is created in solid or liquid phases containing Ra. It is well known that radioactive nuclides in the U-238 decay chain occur in the Earth's crust with varying degrees of concentration and can be found almost in all types of soil, rocks, granite, and sand (Kobeissi et al. 2008; 2013). Specifically, Rn emits alpha particles with energy 5.8 MeV and is the most important radioactive element that can move through the Earth's crust with a half-life of 3.82 days and reach the atmosphere and local surroundings (Nazaroff et al. 1988).

An additional property of Rn gas is its recoil energy, which enables it to migrate varying distances in porous and permeable media, thus allowing it to escape into the atmosphere from the subsurface. The migration and the transport of Rn from a geological formation into its surroundings depend on the structure of the geological medium and its permeability and porosity. Its movement also depends on the grain packing in rocks, the type of crystal lattice and granite types in the study area (Kobeissi et al. 2013), surface and subsurface characteristics, the soil moisture content in different types of rocks, and soil-air pressure differences. An additional property of Rn is its solubility in ground water, which allows it to be transported to greater distances, while its half-life might not allow it to do so. All these factors must be taken into consideration when Rn is used as a precursor for the occurrence of earthquakes and the interpretation of data.

Ra-226, with a half-life of 1600 years, decays to Rn and also emits alpha particles as well as gamma (γ)-rays.

Therefore the presence and amount of Ra in soil subsurface determines the number of radon atoms formed in terrestrial crustal layers. The correlation between Rn and Ra concentrations can be useful in measuring Rn and Ra concentration rates from the Earth's surface and subsurface.

2.2 Experimental Field Work

Two profiles stations, Profile-A and Profile-B, for Rn measurements were constructed at two sites of different soil structure inside the same soil formation on the Yammouneh Fault trace (red) in south Lebanon in the location area denoted as C in Fig. 2. Figure 2 shows also details of Profile-A and Profile-B lines crossing the Yammouneh Fault trace (white line).

One profile was set in a homogenous terrain in El-Khiam basin, denoted as Profile-A, and the other was set in a non-homogenous terrain in the village of Blat, denoted as Profile-B, with Profile-B located at about 8 km north of El-Khiam basin along the Yammouneh Fault trace. Figure 2 presents both profile lines crossing the Yammouneh Fault trace line (white line).

To study the fault's seismic activity, we used the properties of Rn and the presence of Ra-226 within the geological formations and the appropriate soil structure of the location for Rn measurements. Some researchers concluded that measurements of radon flux density are more sensitive to Rn convective velocity variation than measurements of radon concentration alone and that a homogeneous structure of the studied fault area is required to give a reliable interpretation of data concerning seismic activity and earthquake occurrences (Yakovleva 2003). In our study, concurrent measurements of Rn concentration and Rn flux exhalation rate from the Earth's surface are performed to improve the sensitivity and reliability of the results.

The borehole method was used in the El-Khiam basin, while the trench (ditch) method was used in Blat village terrain (Fig. 2). The choice of the El-Khiam basin, which is located on one segment of the Yammouneh Fault, for

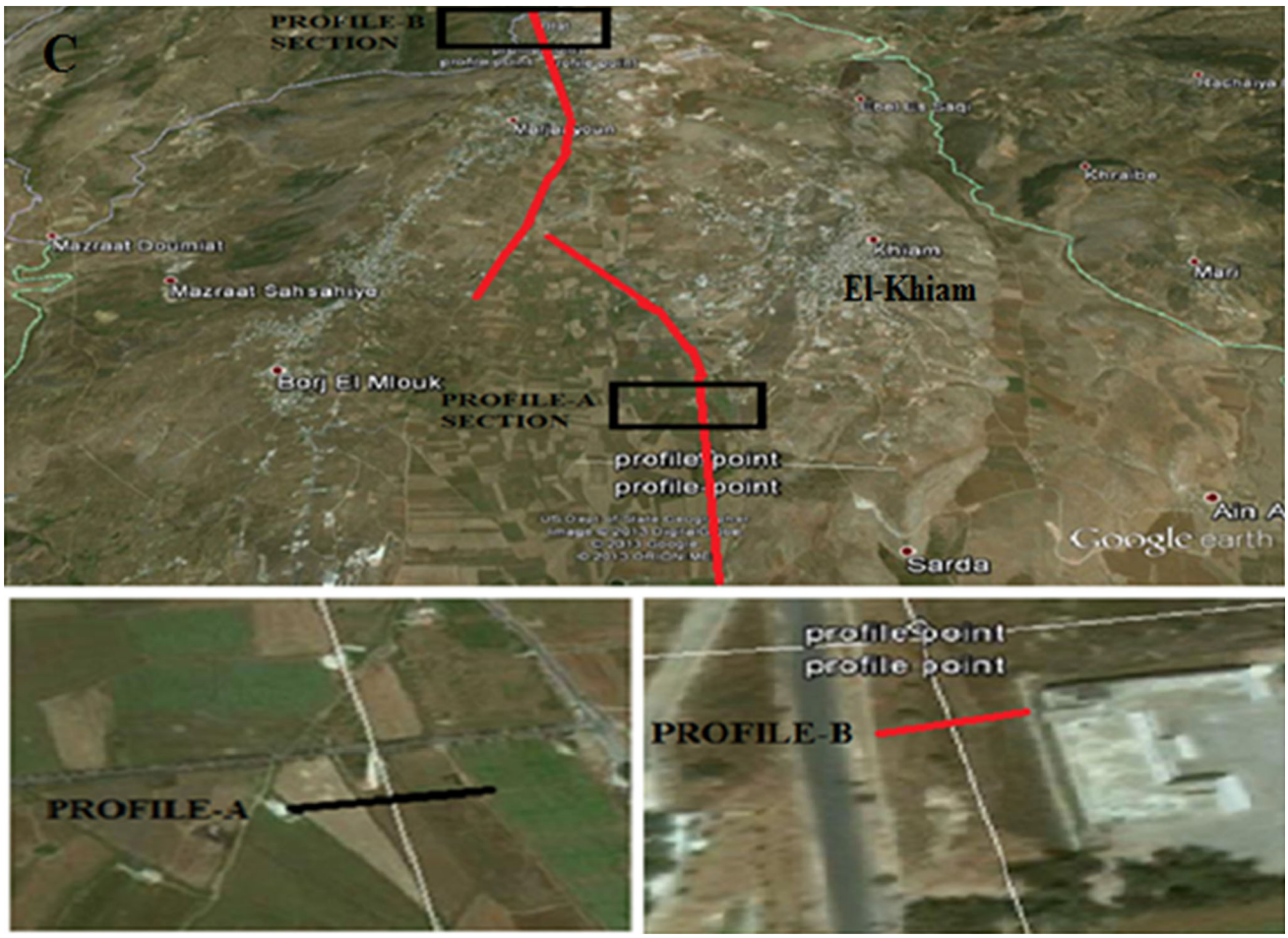

Fig. 2 Study area in a section of south Lebanon (denoted as C) and the trace lines of the Profile-A in El-Khiam basin and Profile-B in Blat village terrain

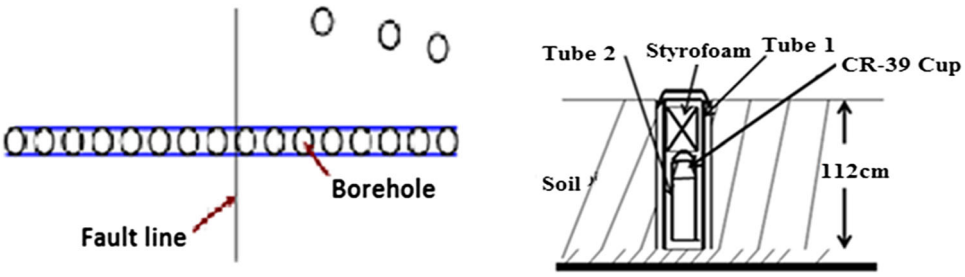

Fig. 3 CR-39 dosimeters distribution and the setup structure of the detection system in the boreholes and the trench

measurement of temporal radon variability, is based on the fault's seismic activity (Gomez et al. 2007), and the required homogeneity of the soil cover present in this location. In addition, the content of Ra-226 in the fault zone and its correlation with the measured Rn emissions can be evaluated. It should be mentioned, that no rainfall occurred during the time of the execution of the experiment. Figure 3 presents the design of the boreholes and the radon measuring system described in Sect. 3.1. Meteorological phenomena, such as lightning, thunder, rainfall, and moisture of the ground and their effects on the measurements, are discussed in Sects. 5.1, 5.3, and 5.6.

3 Experimental Setup and Method of Rn Measurements

In the El-Khiam case the station location was chosen due to the homogeneity of the subsoil and the soil surface. This homogeneity is very important concerning porosity and permeability of the ground for radon emanation. In the case of Blat station, the terrain was somewhat rough and gritty.

3.1 Profile-A in the El-Khiam Basin

The El-Khiam site consists of a basin stretching 15 km in length and about 5 km in width. The soil is fine grainy brown soil with a very thin mixture of very small calcic gravels. Along this profile 21 lined boreholes were drilled (later extended to 29), separated by an interval of 1 m all the way and reaching a depth of 112 cm. The profile line was constructed perpendicular to the Yammouneh Fault trace line, such that the boreholes were distributed in equal number on both sides of the fault trace, as shown in Fig. 3. The three point locations shown off dosimeters line are used for surface soil radon measurements for comparison with fault radon results and as control.

In each borehole a PVC tube with a diameter of 9 cm and a length of 1 m was inserted with slight pressure on the bottom. The empty space between the borehole wall and the tube was closed firmly with the same extracted soil from the ground to maintain soil homogeneity. To measure Rn exhalation rates from the deep surface of the holes and their cumulative concentrations with time, a second PVC tube with a diameter of 5 cm and length of 75 cm was introduced into the first tube. The bottom opening of each tube was wrapped with a plastic mesh to prevent dirt from entering the tubes space. Figure 3 shows the arrangement of the measuring system.

In the inner space and in the top part of the short tube (Tube 2) a CR-39 radon dosimeter detector was inserted, as shown in Fig. 3. Each of the top openings of the tubes was sealed firmly with a screw cover. The space between the two tubes and the space between the tubes screw covers were filled with fiberglass to prevent temperature effects on the measurements. In addition, a thermometer was inserted in the fiberglass insulator to monitor temperature changes, which were checked at each time interval of the measurements. Temperature values varied from 22 to 24 °C.

The top-level end of the outer tube was enclosed by a PVC cylinder of diameter 20 cm and length 30 cm, which was covered by an insulating cement tile to limit outside temperature variations affecting the inside of the tubes. The CR-39 dosimeter, which registers cumulative Rn alpha tracks as described in Kobeissi et al. (2008) and shown in Fig. 3, consists of a plastic cup on whose bottom center a CR-39 detector (with dimensions 20 × 15 mm^2 and 1 mm thick) was fixed by a double sticking material. The center of the cup cover was equipped with a 1 cm diameter hole covered with a 1.5 cm thick sponge filter, through which only Rn gas can penetrate to the interior of the cup. The calibration of the dosimeter was done earlier at the Federal Office for Radiation Protection in Berlin.

For the measurements of radon variability, the CR-39 detectors were exposed to the soil Rn gas for one week intervals starting on 24 July 2013. In the completion of each weekly period (denoted as time interval) of measurement (168 h), the previous dosimeters were removed and replaced by new ones for each borehole.

After exposure, the detectors were etched in a 7 N KOH solution for 210 min at 90 °C to enlarge the latent tracks. The detectors were then rinsed with distilled water and cleaned with alcohol. The tracks were counted under an optical microscope, with magnification depending on the density range of the tracks. Minimal overlaps of tracks could be easily distinguished and counted.

The track counting was performed in 20 views for each detector, which were swept over the detector surface, with at least 50 counts per view to minimize statistical errors and to obtain the tracks density ρ_x (tracks/cm^2). The Rn concentration was obtained by the expression:

$$C_x\left(\mathrm{Bq/m^3}\right) = K\rho_x/t_x, \quad (1)$$

where t_x is the measured time in each time interval and $K = 150$ [(Bq m^{-3}) h (tracks/cm^2)$^{-1}$] is the calibration constant. The radon aerial exhalation rate E_A, emanated from the Earth's surface, is calculated from the following equation (Khan et al. 1992; Sharma et al. 2003; Singh et al. 2008):

$$E_A = (TV\lambda C_x)/(AT_c) \quad (2)$$

where $T_c = [T - (1/\lambda)(\exp(-\lambda T) - 1)]$, T is the exposure time (in hours) of the CR-39 detectors to Rn emanated from the ground surface within the inner PVC tube, λ (h^{-1}) is the Rn decay constant, V (m^3) is the effective volume of Rn in the inner tube, A (m^2) is the cross-sectional area of the soil surface enclosed in the inner tube, and C_x is the Rn concentration obtained from Eq. 1.

3.2 Profile-B in Blat

This station is situated in a pull-apart segment of the Yammouneh Fault in the village of Blat, as shown in Fig. 2. In this station a trench (ditch) about 170 cm deep and 31 m long was dug across the fault trace line. The same system of PVC tubes was used. The tubes were set firmly on the ditch ground surface and their outer walls were covered fully along the trench with the same soil excavated from the ditch to conform with the local ditch soil environment. Radon measurements in the ditch were performed at a depth of 120 cm, which conforms with the nature of the ditch depth. The same procedure for Rn measurements was used as in Profile-A.

4 Providing a Context for Deep Hole and Ditch Rn Measurements

The purpose of Rn measurements is to compare values of Rn concentrations obtained from top soil surface with those obtained from deep ground, in order to justify that any radon anomalous emission is due to seismic phenomenon and not alone from Ra-226 content in the subsurface.

4.1 Rn Measurements on the Top Soil Surface

In addition to the measuring of radon emission from the deep boreholes bottoms and the ditch's deep surface, it is necessary to carry out concurrently radon measurements at selected soil surface points along the profile line near the top closed end of the large tubes in the locations of both profiles. Similarly, Rn measurements at specific points on the top soil surface at distances of about 10, 15, and 20 m off the fault trace line and off the profile line at a depth of about 15 cm were performed at three surface points shown in Fig. 3. For these measurements the same type of dosimeter was used and was enclosed in a cylindrical PVC chamber, 7 cm in length and 9 cm in diameter, with one opening firmly sealed, while the other open end was exposed to the soil surface. These measurements were performed to provide an unambiguous conclusion for the study results.

4.2 Measurements of Porosity and Ra-226 Concentration in the Soil of the Profiles

To relate any possible anomalous emanation of radon obtained from the deep structure of the faults, soil samples extracted from the boreholes and the ditch were taken to measure the porosity, ε, the density of the solid particles, ρ_s, and the dry density, ρ_d, of the soil. For these measurements, we used the hydraulic pressure method to measure the void volume V_v in the crustal soil (for example, the empty spaces between the solid granule particles in the soil sample). The quantities ε, ρ_s, and ρ_d are related by the following equation (Kobeissi et al. 2008):

$$\rho_d = \rho_s(\varepsilon - 1) \quad (3)$$

In addition, since the Radium element Ra is embedded in the soil subsurface and Rn is emitted from Ra as its progeny, measurements of the concentration of Ra-226 were performed on the same soil samples, using the gamma ray spectroscopy method (Kobeissi et al. 2008).

5 Results and Discussion

Results of Rn emission measurements from the boreholes and the trench deep surface and their top surface along the profile lines are discussed in this section. Results obtained from Rn measurements off-fault trace line and off-profile line and anomalous temporal variability of radon emission are evaluated. Meteorological effects are also presented.

5.1 The Rn Concentration and Exhalation Rates in El-Khiam Basin

Table 2 presents the results of total radon cumulative concentration, C_x (kBq m^{-3}), and the cumulative exhalation rates, E_A (kBq m^{-2} h^{-1}) in each weekly time interval.

Table 2 Total Rn concentration, C_x (kBq m^{-3}) and exhalation rates, E_A (kBq m^{-2} h^{-1})

Time interval	Interval code	Setup date	C_x (kBq m^{-3})	E_A (kBq m^{-2} h^{-1})
1A	1A	July 24	1007	13.70
2A	2A	July 28	1104	15.01
3A	3A	August 4	1215	16.53
4A	4A	August 11	1352	18.39
5A	5A	August 18	1319	17.94
6A	6A	August 25	1234	16.78
7A	7A	September 1	1024	13.92
8A	8A	September 8	1253	17.03
9A	(S8A)	September 15	1375	18.70
10A	9A	September 22 (TH)	1727	23.48
11A	10A	September 29	2233	30.37
12A	11A	October 6	2435	33.12
13A	12A	October 13 (EQ)	2215	30.13
14A	13A	October 20	2574	35.01
15A	14A	October 27 (TH)	2145	29.17
16A	15A	November 3	2348	31.93
17A	16A	November 9	1835	24.96
18A	17A	November 16	2155	29.31

The thunder (TH) on 24 September and 30 October and the earthquake (EQ) in the week 13–20 October 2013 are also shown.

Figure 4 presents some typical radon spectra (histograms) obtained from different weekly time intervals and shows the maximum value of Rn concentration at the fault trace line around borehole A13 and the symmetrical distribution on both sides of the fault line.

The symmetry in the spectral shape (histogram) supports the accurate determination of the fault trace and the accurate choice of the station setting on the fault trace line presented by the accumulative increase–decrease in C_x in the detectors range from A1 to A21, especially at the borehole detector A13. This phenomenon gives reliability to the outcome of the experiment.

In addition, we note in Fig. 4 that the shapes of the spectra cover the fault zone width, indicating the zone width size as well as fracturing in the fault line boundary of the measured fault segment. This fracturing can be due to stress and strike-slip movement of the Yammouneh Fault boundaries at that segment. During the measurements and to confirm the presence of the damage zone and its width, the range of the boreholes containing the detectors was extended on both sides of the fault trace line (E1–E4, W1–W4), starting from the 11th week (11th time interval) of measurements as can be seen in Figs. 4 and 5.

Figure 5 displays the last 18th interval spectrum of radon concentration C_x and exhalation rate E_A, both present the width size of the fault. Both C_x and E_A show the same trend in Rn emission. This behavior was the same in all the measurements. Radon concentration changes significantly along the line perpendicular to the fault trace line, reaching its maximum in the direct location of the fault trace line (Fig. 4). These results confirm the location of the fault line as well as the damaged zone width.

According to the spectral shapes (histograms) given in Fig. 5 and the distribution of detectors along the line crossing the fault trace, the width of the damaged zone in this fault location can be estimated to be about 25–30 m wide. This result is consistent with a recent model study by Shipton (Shipton and Cowie 2003), who showed that the damaged zone width extends from 0 to about 30 m, which is close to our results. These authors argued that damage zones are formed at the tips of the slipping patches of the fault zones when these are subject to enhanced stress. Based on that study, off-fault deformations will potentially occur in regions of high stress around the tips of each slip patch if the stress exceeds a critical value at the fault surface.

Figure 6 presents the temporal variability of radon concentration and exhalation rate, which shows the increase in Rn emanation from interval 7A to interval 12A, which is an increase in the order of 1400 kBq m^{-3}. This confirms that the fault segment is experiencing an active stress/strain and energy accumulation along the fault plane system. The active stress/strain and the process of energy accumulation can reach a critical point at which energy is released in the form of seismic waves and consequently producing an earthquake. The figure shows also the drop in concentration and exhalation rate due to the occurrences of earthquakes during the time interval 13A (black arrow) and thunder effect during time interval 15A (red arrow).

In addition, Fig. 6 shows peaks that occur at certain measurement time intervals. The variability of radon exhalation rates and concentration shows maxima and minima indicating that an alternating process of relaxation and stress enhancement is occurring in the fault segment. Similar results were obtained by Candela et al. (2011) in southern Thailand. But this alternation process could be due to other effects as earthquakes and meteorological disturbances, as discussed in the following section.

5.2 Anomalous Temporal Variation of Radon Gas as a Precursor for Earthquakes

Many researchers have discussed radon anomalous variability as a precursor of earthquakes. In addition to the

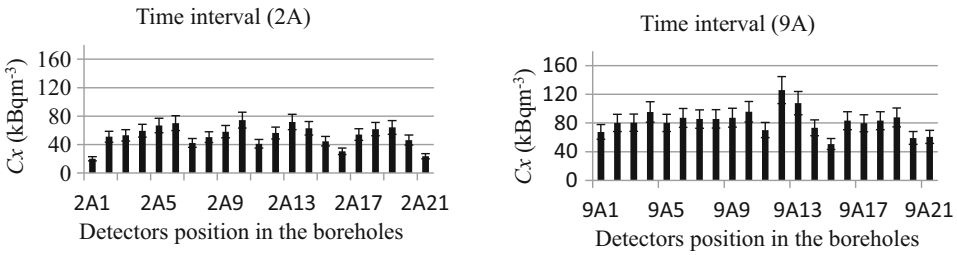

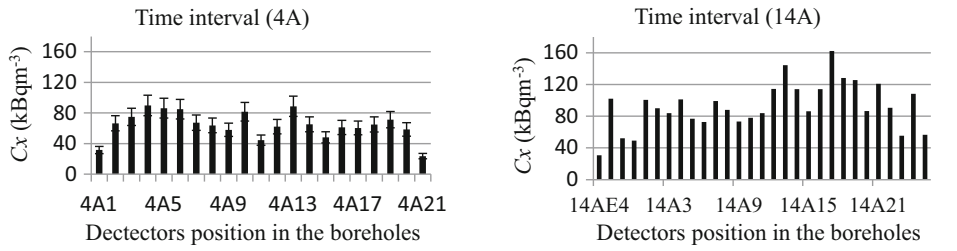

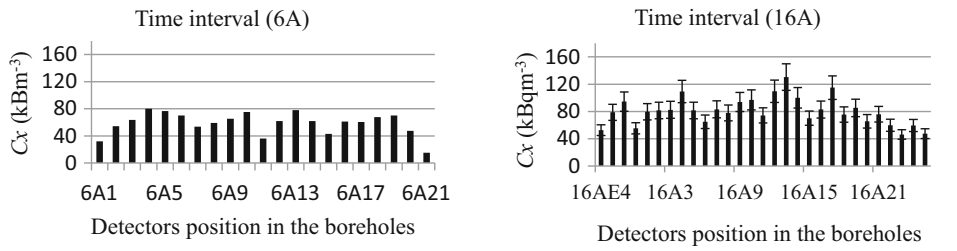

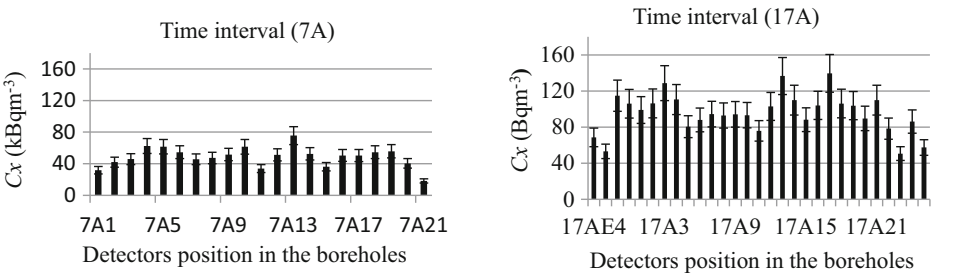

Fig. 4 Typical temporal variation of radon spectra in Profile-A at Yammouneh Fault

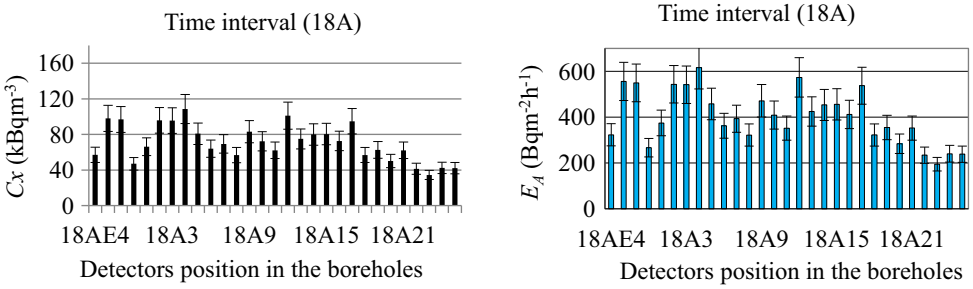

Fig. 5 Rn concentration C_x and exhalation rate E_A in the last time interval

anomalous increase in C_x due to stresses, we observed anomalous phenomenon during the Rn measurements in the 13th weekly time interval 13A as shown in Fig. 6 and Table 2. In this instance Rn concentration dropped about 220 kBq m^{-3} from the preceding value. This drop indicates that the release of energy and stress relaxation in the fault segment boundaries took place, which appears as a seismic wave propagating in the Earth's crust. The correlation between the temporal variation of radon C_x and earthquake is confirmed by our results based on the

occurrence of earthquakes during the Rn measurements as it will be shown in the following.

In Sect. 1 the Yammouneh Fault is described as a branch (splay) of the DSFS that starts in the region of Lake Tiberias in northern Palestine-Israel. During our radon measurements from 13 to 20 October 2013, time interval 13A in Table 2, several earthquakes occurred with the epicenter located in northern Palestine and were felt in the Tiberias region and southwestern Syria as well as in Bent Jbail town in southern Lebanon, which is located southwest of El-Khiam town at a distance of about 28 km and near the border of Palestine. The timing and magnitude of these seismic events are shown in Table 3.

The increase in radon exhalation rate and concentration, starting at the 7th week time interval 7A to the time interval 12A (Table 2; Fig. 6), can be correlated to the increase in the stress and energy storage in the fault boundaries, which produced fracturing in the tips of the fault plates and enhanced permeability of the crust layers for Rn diffusion. But during the time from 13 to 20 October 2013, radon concentration dropped. This drop can be correlated with the drop in the stress and energy release at the fault boundary, which produced seismic waves that affected the emission of radon into the upper layer of the Earth's crust.

The propagation of seismic waves in the fractured medium at a certain time disturbs the enhanced permeability of the fractures. This interpretation is supported by the occurrence of the earthquakes in the Tiberias region as shown in Table 3 during the time between 13th and the 20th October 2013 (time interval 13A) and as shown in Fig. 6 and Table 2. Such seismic wave effect on radon emission has been reported also by Planinić et al. (2004) in Croatia.

The decrease in radon C_x and E_A can be interpreted as being due to the stress drops and the fracturing of the fault plane surfaces, which affects the entropic distributions of the fractures. This hinders instantaneous Rn emission and the diffusion of its carriers to the upper subsurface layers in the Earth's crust. The decrease of radon due to earthquakes is presented also in Fig. 7, where the spectrum of radon concentration has shifted to lower C_x values.

Radon variability is also seen in Fig. 6 and Table 2 where radon concentrations (and thus stresses) recover after the relaxation periods. Therefore, the observed anomalous behavior of radon emanation from the deep ground surface in Profile-A can be interpreted as a precursor of possible earthquake events.

5.3 Meteorological Influence on Rn Emanations from the Earth's Crust

Meteorological phenomena such as lightning and thunder can influence radon temporal behavior. Thunder sound waves might influence the fractured zone in rocks along the fault trace, while moisture due to large content of water in the soil might affect radon penetration through the soil layers. Also it can affect the CR-39 detection surface. Lightning and thunder events occurred during our Rn measurements but there was no rainfall.

The thunder effect is apparent in the drop of radon C_x during the time interval 15A from 27 October to 3

Table 3 Earthquakes in central Levant in north Palestine during 13–20 October 2013

Occurrence (October 2013)	Magnitude	Epicenter
Tuesday, 15	$M = 3.3$	Kinneret, depth 2 km
Thursday, 17	$M = 3.5$	Kinneret
Saturday, 19	$M = 3.5$	North of Kinneret
Sunday, 20	$M = 3.6$	North of Kinneret, depth 5 km (Tiberias)
Sunday, 20	$M = 3.6$	Epicenter south of Ginnosar and Hula Valley

Source European-Mediterranean Seismological Center (n.d.)

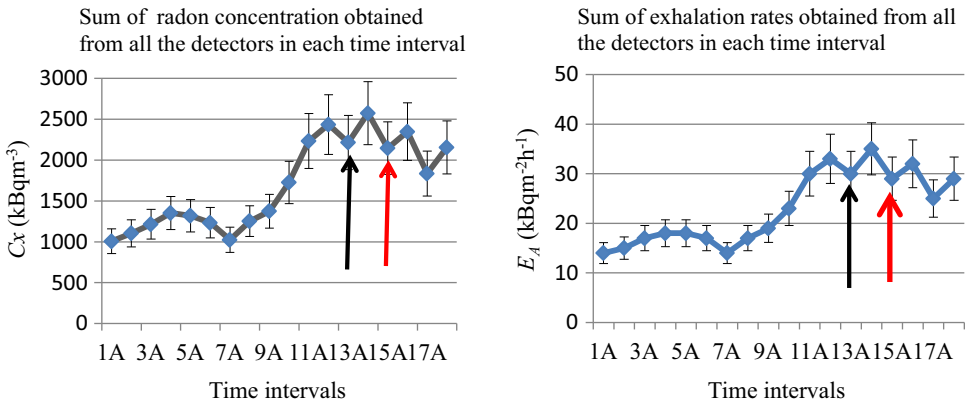

Fig. 6 Temporal variability of radon concentration, C_x and its corresponding exhalation rate E_A. *Arrows* indicate earthquakes effect (*black*) and thunder effect (*red*)

November 2013 when heavy thunder occurred but with no rainfall in the evening of 30 October 2013 at 6 p.m. (Table 2; Fig. 6). This effect of thunder is presented in Fig. 8 as a shift of the spectral line to a lower Rn concentration during measurements in the time interval 15A.

The physical interpretation of the effect of the thunder sound waves can be related to the change in the entropic state of the fractures at the fault plane boundaries, which can hinder the diffusion of radon to the upper soil layers. After the thunder ceased, radon C_x increased within the range of 500 kBq m^{-3}, but remained high. The high C_x and its alternating minima and maxima, shown in Fig. 6, can be interpreted as an indication of alternating stress drops at the fault plane surface, but maintained elevated levels during the rest of the measured time interval.

It must be stated that more work is required to extend the measuring interval times to support such alternation in stress drops. But, clearly thunder sound waves can influence the stress/strain processes and the fractures on the fault line boundary. This can cause a decrease of radon diffusion into the upper layers of the Earth's surface, as did the seismic waves by influencing the fault stress/strain thus decreasing Rn emission into the upper surface of the crust layers.

Based on these results, it is recommended that thunder and its effects be monitored when taking long term measurements of radon emission at the fault trace in order to carefully interpret anomalous behavior or a drop of radon emission. It is also recommended to monitor stress fluctuations by taking measurements in a larger number of time periods during the investigation of fault zones.

5.4 Radon Emission from Boreholes as Compared with Emission from Top Soil Surface Layers

Measurements of radon emission were done at points on the soil surface along the profile line crossing the fault trace and at points off the profile line and off the fault trace line on the ground surface. These measurements were done to compare the temporal behavior of radon emission due to seismic events with natural Rn emission from the ground surface. The results of measurements of radon C_x at the ground surface of the study area are compared with those obtained at the bottom of the boreholes and the trench deep points. The results for Profile-A are shown in Table 4.

Table 4 presents the ratios of Rn concentration obtained from the deep surface of the boreholes, C_xh, to those obtained from the top surfaces of the boreholes, C_xs. The ratios are 5, 13, 15, and 9 for the boreholes AW2, A4, A10, and A15, respectively. Borehole AW2 produced a factor of 5 due to its location just outside the damaged zone of the fault. The higher factors produced within the damaged zone with respect to the zone surface, as seen in Fig. 4, indicate anomalous high Rn emission, which is outside the Rn emission anticipated under natural normal conditions for homogenous soil. Table 4 also presents the ratios of Rn concentration C_xh obtained from deep borehole surfaces to C_xs obtained from the top surface of points, coded L1, L2, and L3 and located outside the damage zone. The ratio of C_xh/C_xs is 5, 9, and 9 for boreholes AW2, A10, and A15, respectively. The ratio of 5 is consistent with the above result for the AW2 top surface, while the higher ratios 9 and 9 for A10 and A15 show Rn anomalous emission due to the presence and the dynamics of the fault trace line. These results are supported also by the averaged C_xh obtained from the boreholes in the range 12A–15A located close to the fault trace line, where this average is 12 times higher than C_xs obtained at soil surface far from the surface area of the damaged zone. These results confirm that the increase in the Rn concentrations and exhalation rates at the fault trace line and the anomalous variation of radon concentrations and exhalation rates are due to the dynamics of the Yammouneh Fault boundary at the studied segment. These results show also that the boreholes methodology is more appropriate for monitoring radon anomalies related to fault tectonic events. This conclusion on the anomalous

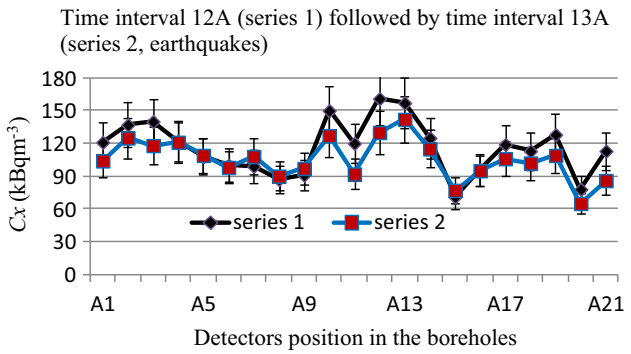

Fig. 7 Shift in the spectrum to lower C_x in the time interval 13A due to earthquakes

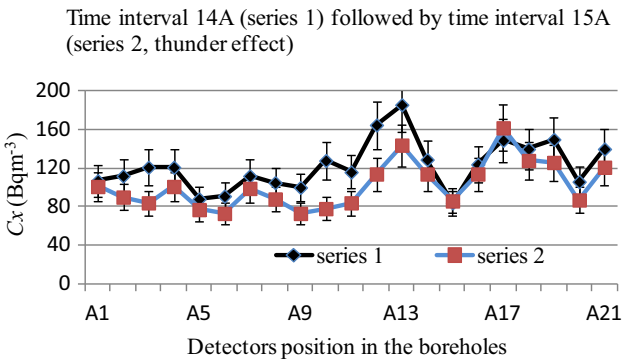

Fig. 8 Shift in the spectrum to lower C_x in the time interval 15A due to weather thunder

Table 4 Results of Rn concentration, C (Bq m^{-3}), obtained from four boreholes positions, AW2, A4, A10, and A15, and from the soil top surface in Profile-A

Time interval		AW2	A4	A10	A15
Rn concentration, C_xh (Bq m^{-3}), taken in the inner surface of borehole chambers					
12A	C_xh	46,254	121,385	126,511	76,694
14A	C_xh	55,352	101,283	77,962	86,178
15A	C_xh	42,767	124,487	116,124	100,205
Average	C_xh	48,124	115,718	106,866	87,692
Time interval		AW2S	A4S	A10S	A15S
Rn concentration, C_xs (Bq m^{-3}), taken at the top surface of the same boreholes					
12A	C_xs	10,563	10,125	8761	14,027
14A	C_xs	13,152	9200	5307	10,515
15A	C_xs	7321	7068	6947	5919
Average	C_xs	10,345	8798	7005	10,154
Ratio	C_xh/C_xs	5	13	15	9
Time interval		L1	–	L3	L2
Rn concentration, C_xs (Bq m^{-3}), taken at the soil surface off the fault and the profile lines (Fig. 3)					
12A	C_xs	7586	–	11,410	13,604
14A	C_xs	12,651	–	16,930	9808
15A	C_xs	7257	–	8187	6682
Average	C_xs	9165	–	12,176	10,031
Ratio	C_xh/C_xs	5	–	9	9

behavior of radon emission at the fault location is also confirmed by the results of the radium Ra-226 measurements in the soil (Sect. 6).

5.5 Profile-B in Blat

In this station, radon measurements at 18 weekly intervals were obtained concurrently with Profile-A measurements. The results for the Rn accumulative concentration and its corresponding exhalation rate obtained from 25 detectors are presented in Table 5.

Table 5 shows the total sum of Rn concentration, C_x (kBq m^{-3}) and the corresponding exhalation rates, E_A (kBq m^{-2} h^{-1}), obtained from all detectors in each weekly time interval. Thunder (TH) occurred on 24 September and 30 October and earthquake (EQ) occurred in the week 13–20 October 2013 and spectral histograms of radon concentrations for some time intervals are shown in Fig. 9 and Rn temporal variations are presented in Fig. 10.

Unlike the case at the fault segment in Profile-A, Table 5 and Fig. 9 show much lower intensity of Rn emissions than those obtained in Profile-A and show also no anomalous increase in the temporal emanation of Rn occurred at this station during the periods of measurement, as indicated in Fig. 10. The absence of increased Rn emanation indicates a possible absence of active stress/strain in this segment of the fault. This lack of stress increase can be explained by the fact that the Yammouneh Fault trace line at Profile-B's location is preceded by a pull-apart segment (Fig. 2) along the fault between the two profiles stations, which might prevent extension of active stress to the next segment. In addition, the amplitude of the seismic wave due to the earthquake of magnitude 3.6, as listed in Table 3, might have been subject to damping with energy loss in the crustal layer, and therefore did not reach the location of Profile-B.

This absence of a radon signal during the earthquakes is supported by the sensitivity of the fault at Profile-B to the sound wave vibration of thunder during the measurements, while this sensitivity did not appear for seismic waves at Profile-B, as discussed in Sect. 5.6.

5.6 Meteorological Effects

The two maxima of Rn concentration shown in Fig. 10 are produced by the sound waves of the thunder, which occurred on 24 September, during time interval 9B (22–29 September) and on 30 October during time interval 14B (27 October–3 November 3), as presented in Table 5, Figs. 9 and 10.

Thunder sound waves during the Rn measuring interval periods have increased radon emission as shown in the spectral shifts presented in Fig. 11. This effect of thunder produced about a 56 % increase in Rn concentration

intensity. This meteorological phenomenon concurrently affected radon emanation in both profiles. The absence of a shift in the spectrum between the 11th and the 14th detectors in the time interval 13B (Fig. 11) is due to the presence of a large rocky area under the detectors in that section. This effect justifies the choice of the location with homogenous terrain to execute such studies using soil gases emanation from the ground near faults traces in order to obtain reliable interpretation of the data.

Based on the results of the thunder effect, we conclude that the earthquakes did not affect the Yammouneh Fault segment at Profile-B, as the quakes did along Profile-A in the El-Khiam basin. In addition, there was no indication in the data of active stress/strain accumulation in this segment of the fault beside its normal strike-slip action.

5.7 Radon Emanation from the Upper Soil Surface of Profile-B

For these measurements of radon, the same procedure was followed as was done for Profile-A, except that the depth here is greater due to a deeper trench. Table 6 shows the radon concentration obtained from about 120 cm below the surface within the PVC tube in the trench and Rn concentrations obtained from points at the top surface of the profile line and from points off the Profile-B line further away from the fault trace line.

The ratios were between Rn concentrations obtained from the deep surface under the tubes and those obtained from the top surface. These ratio values are 2, 2, 2, and 1.3 for the detectors locations B6, B15, B19, and B29, respectively. Similarly, results were obtained for the location points B2, B3, and B1 off the fault trace line with ratios 1.5, 2, and 2, respectively. These results indicate a natural diffusion process of radon and the absence of seismic effects on that segment of the fault.

Unlike the case in El-Khiam along Profile-A, radon temporal exhalation rates and concentrations in Profile-B remained approximately at the same levels during the measurements, except those times during which thunder occurred, which produced maximal levels of radon emission as shown in Figs. 9 and 10. No other anomalous temporal variation in radon concentrations was observed along this segment of the fault. Thus, a comparison between the results obtained in both profiles located at different locations (segment) leads us to conclude that Rn concentrations showing high rates obtained at the fault in Profile-A are due to seismic activity along the fractured segment boundaries of the Yammouneh Fault. This means that segments of a fault can show different stress/strain behavior.

Table 5 Radon concentration and exhalation rates along Profile-B

Time interval	Interval code	Interval date	C_x (kBq m^{-3})	E_A (kBq m^{-2} h^{-1})
1B	1B	July 28	172	2.34
2B	2B	August 4	199	2.71
3B	3B	August 11	238	3.23
4B	4B	August 18	195	2.66
5B	5B	August 25	178	2.43
6B	6B	September 1	164	2.23
7B	7B	September 8	175	2.38
8B	S7B	September 15	185	2.52
B9 (TH)	8B	September 22	289	3.94
10B	9B	September 29	246	3.35
11B	10B	October 6	157	2.13
B12 (EQ)	11B	October 13	182	2.48
13B	12B	October 20	189	2.57
B14 (TH)	13B	October 27	384	5.22
15B	14B	November 3	259	3.52
16B	15B	November 9	217	2.95
17B	16B	November 16	260	3.53
18B	17B	November 23	315	4.28

6 Determination of Porosity (ε) and Ra-226 Concentration in the Profiles Soil

As stated in Sect. 5, measurements of porosity, ε, the solid density, ρ_s, and the dry soil density, ρ_d, of soil samples were performed. In addition, measurements of Ra-226 concentrations were carried out on the same soil samples, using gamma-ray methodology (Kobeissi et al. 2008). Table 7 shows the results of the measurements of radium concentration C_{Ra} (Bq kg^{-1}), porosity, ε, density ρ_s, and density ρ_d of some soil samples taken from the deep surface of the boreholes and the deep trench surface as well as from the top surface of both profiles.

It can be seen that Ra concentrations are comparable with those obtained for gray cement (73.2 ± 3 Bq kg^{-1}) and white cement (76.3 ± 3 Bq kg^{-1}), but are somewhat higher than those obtained from sand grain soil, which range from 4.2 to 60.8 Bq kg^{-1} (Kobeissi et al. 2008). These same Ra values are lower than the values obtained for granite, which range between 2 and 494 Bq kg^{-1} (Kobeissi et al. 2013). This lower value of Ra in the soil of both profiles is because the presence of granite in this subsurface is not significant.

Concentration C_{Ra} (Bq kg^{-1}) of Ra as an emitter of Rn in the soil samples, taken from the study area, is characterized by small variations compared to those of Rn emission shown in Table 2. In addition, the porosities values obtained from the samples taken from the sites of the two profiles are comparable with those obtained in sand grain samples, which ranged between 0.465 and 0.624 (Kobeissi et al. 2008).

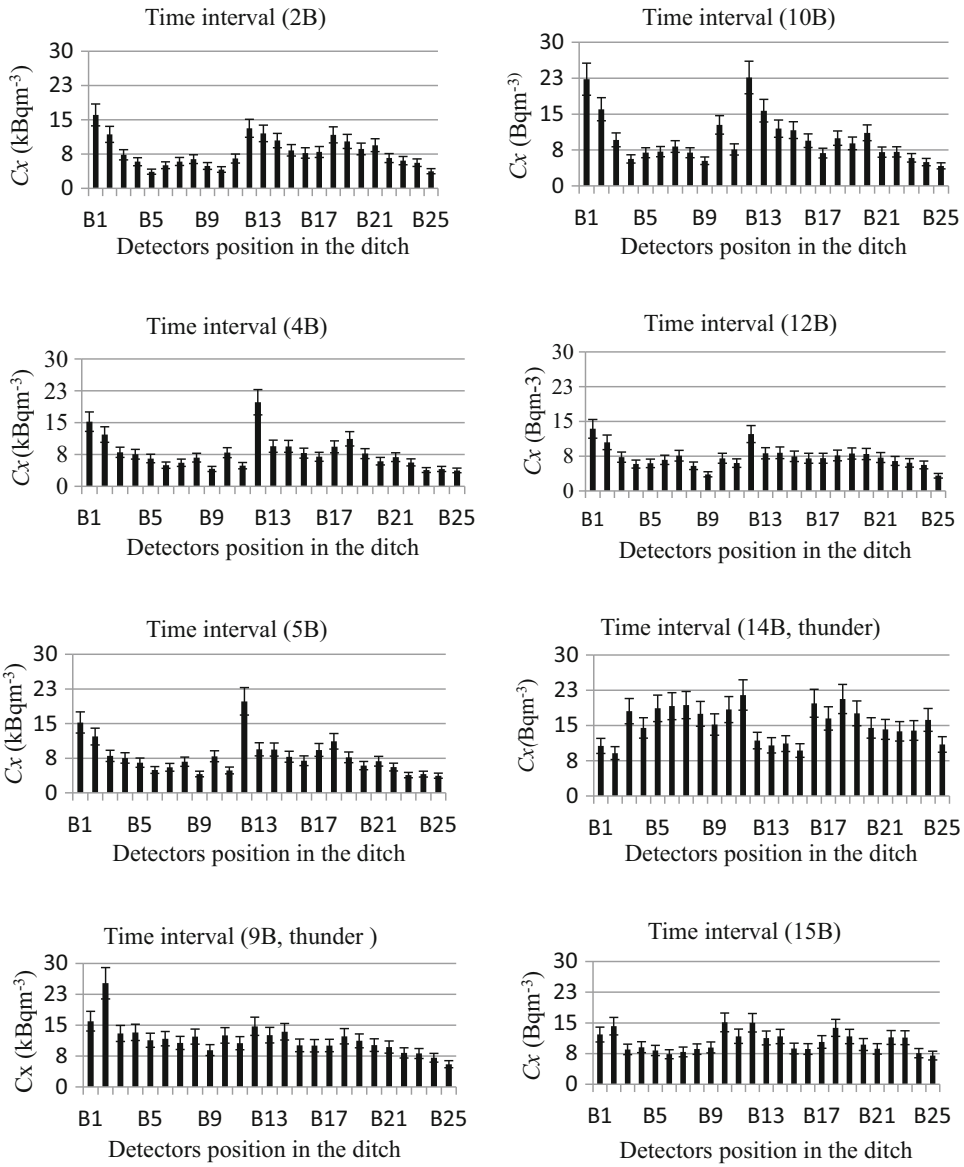

Fig. 9 Rn spectra for some time intervals in Profile-B. The spectral level increased during the time intervals 9B and 14B

These results of Ra content in the soil of the study area and the low values of radon emanation in Profile-B conform to the naturally occurring average Ra concentration in the profiles locations and confirm that the high radon concentration and variability, obtained in the Profile-A location, is produced by seismic stress/strain action at the boundary of the study segment of the Yammouneh Fault in south Lebanon.

7 Evaluation of Some Geophysical Parameters in the El-Khiam Basin

Based on the results obtained in this study, it is appropriate to extract and evaluate some geophysical properties related to the nature of the studied area in El-Khiam basin, such as the Crustal Structure Parameter, the Gaseous Geoseismicity, and the Effectiveness Parameter to Detect Seismic Waves.

(1) Our measurement of the precursory radial distance, D, between the epicenter of the October 2013 earthquake swarm, which was located at the village of Keneret in the Tiberias region, and the Profile-A location in the El-Khiam basin, is close to $D = 68$ km. Using this value of D, the size of the zone can be estimated by the relation (Planinić et al. 2004)

$$D = ae^{M} \tag{4}$$

where M is the earthquake magnitude and a is a parameter whose value is ≥ 1, depending on the crustal structure of the studied location. By using the value of M listed in Table 3 and the value of D, we obtain $a = 1.9$ for El-Khiam basin.

This value of a implies that the detectors planted in Profile-A in El-Khiam basin are sensitive to seismic waves of magnitude $M = 3.6$ at a radial distance $D \leq 68$ km. This result is supported by the fact that the detected earthquakes (Table 3) noted during our measurement period were also felt in the town of Bent Jbail in south Lebanon, located southwest at a distance of 28 km from EL-Khiam basin within that radial zone. This possible detection cannot be asserted, because the crustal structure might vary within the seismic zone and can affect the value of the parameter a. This zone dimension could also be the reason why seismic waves were not detected at Profile-B in Blat, which is located outside the detection zone in an area where this fault segment lacked the presence of stress/strain action along the fault planes, as was discussed in the case of Profile-B.

(2) Another factor that can be deduced from our results is the Gaseous Geoseismic Parameter, where the relation between the epicenter distance, D (km), the magnitude M, and the precursory time T is given as:

$$\log(DT) = 0.63M + b \quad (5)$$

where b is a parameter related to the gaseous geoseismic precursor of earthquakes (Planinić et al. 2004). From our data, b was calculated and found as $b = 1.1$ (T (28 days) is the starting time at which C_x began to increase and the time at which C_x began to drop at the occurrence point of the earthquakes). This value is in contrast with value found by Planinić as 1.68 for eastern Croatia (Planinić et al. 2004). This difference could be due to the difference in the geological formation and structure of Earth's crust of the studied areas.

(3) Another property that can be extracted from the results of our study is the earthquake effectiveness

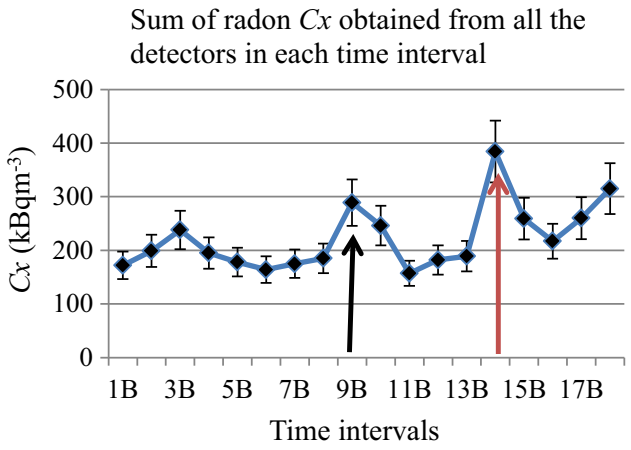

Fig. 10 Rn variation of C_x (kBq m^{-3}). Thunder effect on Rn emission indicated by the *arrows*

Table 6 Rn concentration C_x (Bq m^{-3}) in the trench detectors of Profile-B in time intervals 11B, 13B, and 14B

Time interval		B6	B15	B19	B29
Radon C_xh produced in the inner space of the boreholes chamber					
11B	C_xh	6713	7480	7972	9598
13B	C_xh	19,124	9692	14,502	9823
14B	C_xh	7353	8745	9697	11,866
Average	C_xh	11,063	8639	10,724	10,429

Time interval	CR-39 Code	B6S (UP)	B15S	B20S	B29S (UP)
Radon C_xs taken at four points on the surface of the trench line soil					
11B	C_xs	3663	1277	2409	9557
13B	C_xs	11,334	8443	6353	8165
14B	C_xs	5337	4823	5719	6195
Average	C_xs	6778	4848	4827	7972
Ratios	C_xh/C_xs	2	2	2	1.3
Time interval	CR-39 code	B2	B3	–	B1
Radon C_xs taken at the outside of Profile-B at three locations					
11B	C_xs	5106	3677	–	3034
13B	C_xs	12,991	–	–	9447
14B	C_xs	5129	4437	–	3250
Average	C_xs	7742	4057	–	5244
Ratios	C_xh/C_xs	1.5	2	–	2

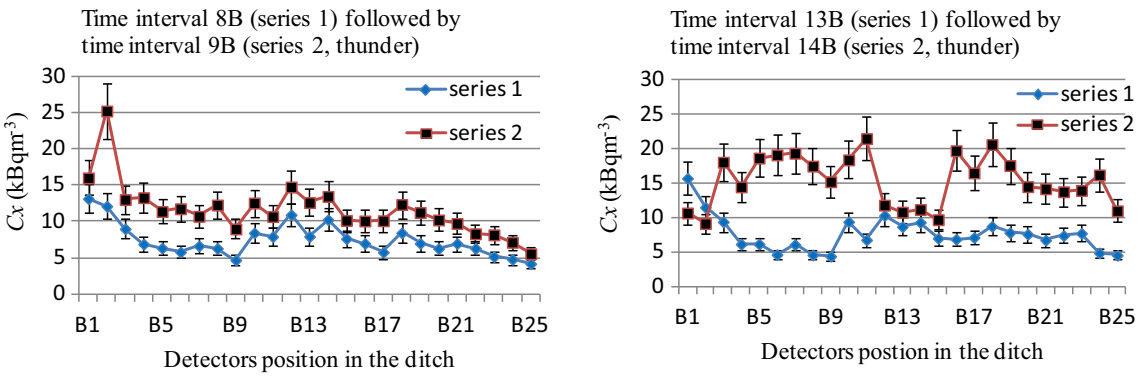

Fig. 11 Spectral shift of radon concentration due to the thunder effect on radon emission

Table 7 Ra concentration C_{Ra} (Bq kg^{-1}), porosity ε and densities ρ_d and ρ_s, of soil samples

	ρ_d	ρ_s	ε	C_{Ra} (Bq kg^{-1})
El-Khiam Profile-A				
K11 (surface soil)	1.2	2.33	0.485	86 ± 8
KO (surface soil)	1.1	2.30	0.565	89 ± 11
K13 (surface soil)	1.3	2.63	0.544	90 ± 10
K15 (surface soil)	1.2	2.1	0.43	80 ± 8
Deep hole soil samples	LB-kX-10	LB-k15	LB-kx2-15	
C_{Ra} (Bq kg^{-1})	68 ± 6	80 ± 8	90 ± 10	
Blat Profile-B (ditch surface granular soil samples)				
B1 (surface soil)	1.0	1.95	0.487	60 ± 5
B2 (surface soil)	1.1	2.2	0.5	
Deep ditch soil samples	LB-BX-1 (brown)	LB-BX-2 (yellow)	LB-BX-3 (brown)	
C_{Ra} (Bq kg^{-1})	41 ± 6	40 ± 6	50 ± 3	

parameter η, which is the potential to detect seismic events in the El-Khiam basin—a property and ability of the applied detection system in this work. This factor can be calculated using the relation (Planinić et al. 2004):

$$\eta = 10^{(1.3M-8.19)}/D^3 \quad (6)$$

Using the values of $M = 3.6$ and $D = 68$ km, we obtain $\eta = 9.8 \times 10^{-10}$, which is comparable to the values 1.4×10^{-10}, 1.6×10^{-10}, 8.1×10^{-10}, and 8.2×10^{-11} obtained at some locations for Croatian soil (Planinić et al. 2004). This obtained value and its closeness with other published values of similar measuring system give confidence and reliability in our monitoring system.

8 Conclusions

The conclusions that we draw from this study are that:

(1) Soil radon gas emanation along fault traces can be used as a possible precursor for earthquake prediction, as was confirmed by the correlation of radon increase in radon exhalation rates and the occurrence of earthquakes in the Tiberias region in northern Palestine;
(2) An increase of radon temporal emission is correlated with stress/strain and energy accumulation along the fault system boundaries, as an indicator for possible earthquake occurrence;
(3) The results of the measurements indicate that the lag time of the occurrence of earthquakes is on the order of a few weeks but can be longer;
(4) Radon spectral line width reflects the presence of a fault damage zone across the fault trace line, which indicates the presence of fracturing of the border zone between the fault planes. This is due to the action of the stresses and shearing processes along the boundaries of the Yammouneh Fault in south Lebanon, which allows the fault zone width to be estimated;
(5) Meteorological effects on radon emission, such as thunder, can influence the stress on the fault planes boundary;
(6) Terrain homogeneity in the study area is needed to obtain a reliable interpretation of the measured data; and
(7) Longer periods of measurement are required to better understand the correlation between fault stress/strain and radon emission at the fault trace location.

Acknowledgments The financial support of the Lebanese National Council for Scientific Research is appreciated. Thanks go to Dr. O. El-Samad for the use of his laboratory for the gamma measurements. We appreciate as well the assistance of the municipality heads of the towns of El-Khiam and Blat. Our deep thanks go to Mr. Rabah Faour and Mr. Sameeh Ramadan for providing their land lots to establish the profile stations. The corresponding author would like to thank Professor H. Gould at Clark University for helping to edit the manuscript and Professor R. Reilinger at MIT for useful comments. The assistance and the hard work of Miss Fatima Jaffal, a graduate student at the Physics Department, Faculty of Sciences of the Lebanese University, is highly appreciated.

References

Alchalbi, A., M. Daoud, F. Gomez, S. McClusky, R. Reilinger, M.A. Romeyeh, A. Alsouod, R. Yassminh, et al. 2009. Crustal deformation in northwestern Arabia from GPS measurements

in Syria: Slow slip rate along the northern Dead Sea Fault. *Geophysical Journal International* 180(1): 125–135.

Ambraseys, N.N., and C.P. Melville. 1988. An analysis of the eastern Mediterranean earthquake of 20 May 1202. In *History of seismography and earthquakes of the world*, ed. W.K.H. Lee, H. Meyers, and K. Shimazaki, 181–200. San Deigo: Academic Press.

Baykut, S., T. Akgul, and S. Inan. 2011. Seismic activity-related anomaly detection in soil radon emanation. In *Proceedings of the 19th European signal processing conference, EUSIPCO 2011*, Barcelona, Spain, 908–912.

Beydoun, Z.R. 1999. Evolution and development of the Levant (Dead Sea Rift) transform system: A historical-chronological review of a structural controversy. In *Continental tectonics*, vol. 164, ed. C. MacNiocaill, and P.D. Ryan, 239–255. London: Geological Society of London.

Bhongsuwan, T., P. Pisapak, and H. Duerast. 2011. Result of alpha truck detection of radon in soil gas in the Khlong Marui Fault Zone, southern Thailand: A possible earthquake precursor. *Songklanakarin Journal of Science and Technology* 33(5): 609–616.

Butler, R.W.H., S. Spencer, and H.M. Griffiths. 1998. The structural response to evolving plate kinematics during transpression: Evolution of the Lebanese restraining bend of the Dead Sea transform. In *Continental transpressional and transtensional tectonics*, Special Publications, vol. 135, ed. R.E. Holdsworth, R.A. Strahan, and J.F. Dewey, 81–106. London: Geological Society of London.

Butler, R.W.H., and S. Spencer. 1999. Landscape evolution and the preservation of tectonic landforms along the northern Yammouneh Fault, Lebanon. In *Uplift, erosion and stability: Geological and geomorphological perspectives on landscape evolution*, Special Publication, vol. 162, ed. B.J. Smith, W.B. Whalley, and P.A. Warke, 143–156. London: Geological Society of London.

Candela, T., F. Renard, M. Bouchon, J. Schmittbuhl, and E.E. Brodsky. 2011. Stress drop during earthquakes: Effect of fault roughness scaling. *Bulletin of the Seismological Society of America* 101(5): 2369–2387.

Daeron, M., L. Benedetti, P. Ttapponier, A. Sursock, and R. Finkel. 2004. Constraints on the post-25-ka slip rate of the Yammouneh fault (Lebanon) using in situ cosmogenic 36-Cl dating of offset limestone-clast fans. *Earth and Planetary Science Letters* 227(1–2): 105–119.

Daeron, M., Y. Klinger, P. Ttapponier, A. Elias, E. Jacques, and A. Sursock. 2005. Sources of the large A.D. 1202 and 1759 near East earthquakes. *Geology* 33(7): 529–532.

Daeron, M., Y. Klinger, P. Tapponnier, A. Elias, E. Jacques, and A. Sursock. 2007. 12,000-year long record of 10 to 13 paleo-earthquakes on the Yammouneh Fault (Levant Fault System, Lebanon). *Bulletin of the Seismological Society of America* 97: 749–771.

Darawcheh, R., M.R. Sbeinati, C. Margotti, and S. Paolini. 2000. The 9 July 551 AD Beirut earthquake, Eastern Mediterranean region. *Journal of Earthquake Engineering* 4(4): 403–414.

Elias, A., P. Tapponnier, S.C. Singh, G.C.P. King, A. Briais, M. Daeron, H. Carton, A. Sursock, et al. 2007. Active thrusting offshore Mount Lebanon: Source of the tsunamigenic A.D. 551 Beirut-Tripoli earthquake. *Geology* 35(8): 755–758.

Erees, F.S., S. Aytas, M.M. Sac, G. Yener, and M. Salk. 2007. Radon concentrations in thermal waters related to seismic events along faults in the Denizli Basin, Western Turkey. *Radiation Measurements* 42(1): 80–86.

European-Mediterranean Seismological Center. n.d. http://www.emsc-csem.org. Accessed May 2015.

Freund, R., Z. Garfunkel, I. Zak, M. Goldberg, T. Weissbrod, and B. Derin. 1970. The shear along the Dead Sea rift. *Philosophical Transactions A* 267(1181): 107–130.

Gomez, F., M. Meghraoui, A. Darkal, R. Sbeinati, R. Darawcheh, C. Tabet, M. Khawlie, M. Charabe, et al. 2001. Coseismic displacements along the Serghaya fault: An active branch of the Dead Sea fault system in Syria and Lebanon. *Journal of the Geological Society* 158: 405–408.

Gomez, F., M. Meghraoui, A. Darkal, F. Hijazi, M. Mouty, Y. Suleiman, R. Sbeinati, R. Darawcheh, et al. 2003. Holocene faulting and earthquake recurrence along the Serghaya branch of the Dead Sea fault system in Syria and Lebanon. *Geophysical Journal International* 153(3): 658–674.

Gomez, F., M. Khawlie, C. Tabet, A.N. Darkal, K. Khair, and M. Barazangi. 2006. Late Cenozoic uplift along the northern Dead Sea transform in Lebanon and Syria. *Earth and Planetary Science Letters* 241: 913–931.

Gomez, F., T. Nemer, C. Tabet, M. Khawlie, M. Meghraoui, and M. Barazangi. 2007. Strain partitioning of active transpression within the Lebanese restraining bend of the Dead Sea fault (Lebanon and SW Syria). In *Tectonics of strike-slip restraining and releasing bends in continental and oceanic settings*, Special Publication, vol. 290, ed. D. Cunningham and P. Mann, 285–303. London: Geological Society of London.

Khair, K. 2001. Geomorphology and seismicity of the Roum fault as one of the active branches of the Dead Sea fault system in Lebanon. *Journal of Geophysical Research* 106: 4233–4245.

Khan, J., R. Prasad, and R.K. Tyagi. 1992. Measurements of exhalation rate from some building materials. *Nuclear Tracks Radiation Measerments* 36: 465–469.

Kobeissi, M.A., O. El-Samad, K. Zahraman, S. Milki, F. Bahsoun, and K.M. Abumurad. 2008. Natural radioactivity measurements in building materials in southern Lebanon. *Journal of Environmental Radioactivity* 99: 1279–1288.

Kobeissi, M.A., O. El-Samad, and I. Rachidi. 2013. Health assessment of natural radioactivity and radon exhalation rate in granites used as building materials in Lebanon. *Radiation Protection Dosimetry* 153(3): 342–343.

Kuo, T., C. Lin, K. Fan, G. Chang, C. Lewis, and Y. Han. 2009. Radon anomalies precursory to the 2003 Mw = 6.8 Chengkung and 2006 Mw = 6.1 Taitung earthquakes in Taiwan. *Radiation Measurements* 44(3): 295–299.

McKenzie, D. 1972. Active tectonics of the Mediterranean region. *Geophysical Journal of the Royal Astronomical Society* 30(2): 109–185.

Meghraoui, M., F. Gomez, R. Sbeinati, J. Van der Woerd, M. Mounty, A.N. Darkal, Y. Radwan, I. Layyous, et al. 2003. Evidence for 830 years of seismic quiescence from palaeoseismology, archaeology and historical seismicity along the Dead Sea fault in Syria. *Earth and Planetary Science Letters* 210: 35–52.

Mohamad, R., A.N. Darkal, D. Seber, E. Sandvol, F. Gomez, and M. Barazangi. 2000. Remote earthquake triggering along the Dead Sea fault in Syria following the 1995 Gulf of Aqaba earthquake (Ms = 7.3). *Seismological Research Letters* 71(1): 47–52.

Nazaroff, W.W., B.A. Moed, and R.G. Sextro. 1988. Soil as a source of indoor radon: Generation, migration and entry. In *Radon and its decay products in indoor air*, ed. W.W. Nazaroff, and A.V. Nero, 57–112. New York: Wiley.

Nemer, T., and M. Meghraoui. 2006. Evidence of coseismic ruptures along the Roum fault (Lebanon): A possible source for the AD 1837 earthquake. *Journal of Structural Geology* 28: 1483–1495.

Nemer, T., M. Meghraoui, and K. Khair. 2008. The Rachaya-Serghaya fault system (Lebanon). Evidence of Coseismic ruptures and the AD 1759 earthquake sequence. *Journal of*

Geophysical Research 113(B5): 1978–2012. doi:10.1029/2007JB005090.

Nemer, T., F. Gomez, S. Al Haddad, and C. Tabet. 2008. Coseismic growth of sedimentary basins along the Yammouneh strike-slip fault (Lebanon). *Geophysical Journal International* 175(3): 1023–1039.

Palano, M., P. Imprescia, and S. Gresta. 2013. Current stress and strain-rate fields across the Dead Sea Fault System: Constraints from seismological data and GPS observations. *Earth and Planetary Science Letters* 369–370: 305–316.

Papp, B., F. Deák, Á. Horváth, Á. Kiss, G. Rajnai, and Cs Szabo. 2008. A new method for the determination of geophysical parameters by radon concentration measurements in bore-hole. *Journal of Environmental Radioactivity* 99: 1731–1735.

Planinić, J., V. Radolić, and B. Vuković. 2004. Radon as an earthquake precursor. *Nuclear Instruments and Methods in Physics Research A* 530(3): 568–574.

Plassard, J., and B. Kogoj. 1981. *Seismicity of Lebanon* (*Seismicite du Liban: catalogue des seismes ressentis*), 3rd edn. Beyrouth: Conseil National de Recherche Scientifique.

Reilinger, R., S. McClusky, P. Vernant, S. Lawrence, S. Ergintav, R. Cakmak, M. Nadariya, G. Hahubia, et al. 2006. GPS constraints on continental deformation in the Africa-Arabia-Eurasia continental collision zone and implications for dynamics of plate interactions. *Journal of Geophysical Research* 111: 1978–2012. doi:10.1029/2005JB004051.

Richon, P., Y. Klinger, P. Tapponnier, C.X. Li, J. Van Der Woerd, and F. Perrier. 2010. Measuring radon flux across active faults: Relevance of excavating and possibility of satellite discharges. *Radiation Measurements* 45(2): 211–218.

Sbeinati, M.R., R. Darawcheh, and M. Mouty. 2005. Catalog of historical earthquakes in and around Syria. *Annals of Geophysics* 48: 347–435.

Sharma, D.K., A. Kumar, M. Kumar, and S. Singh. 2003. Study of uranium, radium and radon exhalation rate in soil samples from some areas of Kangra district, Himashal Pradesh, India using solid-state nuclear track detectors. *Radiation Measurements* 36: 363–366.

Shipton, Z.K., and P.A. Cowie. 2003. A conceptual model for the origin of fault damage zone structures in high-porosity sandstone. *Journal of Structural Geology* 25: 333–344.

Singh, H., J. Singh, S. Singh, and B.S. Bajwa. 2008. Radon exhalation rate and uranium estimation study of some soil and rock samples from Tusham ring complex, India using SSNTD technique. *Radiation Measurements* 43(S1): S459–S462.

Tapponnier, P., M. Daeron, G. King, E. Jacques, A. Sursock, and A. Elias. 2001. Active faulting and seismic hazard in Lebanon. *Journal of Conference Abstracts* 6: 1988 (EUG XI abstracts).

Walia, V., T.C. Su, C.C. Fu, and T.F. Yang. 2005. Spatial variation of radon and helium concentration in soil-gas across the Shan-Chiao fault, Northern Taiwan. *Radiation Measurements* 40: 513–516.

Walia, V., T.F. Yang, W.-L. Hong, S.-J. Lin, C.-C. Fu, K.-L. Wen, and C.-H. Chen. 2009. Geochemical variation of soil-gas composition for fault trace and earthquake precursory studies along the Hsincheng fault in NW Taiwan. *Applied Radiation and Isotopes* 67: 1855–1863.

Walley, C.D. 1988. A braided strike-slip model for the northern continuation of the Dead Sea Fault and its implications for Levantine tectonics. *Tectonophysics* 145: 63–72.

Yakovleva, V.S. 2003. The radon flux density from the Earth's surface as an indicator of seismic activity. In *Proceedings of ICGG7*, Copernicus GmbH, 28–30.

Yang, T.F., C.Y. Chou, C.-H. Chen, L.L. Chyi, and J.H. Jiang. 2003. Exhalation of radon and its carrier gases in SW Taiwan. *Radiation Measurements* 36: 425–442.